Earthquake Science
地震学报 英文版 ISSN 1674-4519 CN 11-5695/P

Acoustic finite-difference modeling beyond conventional Courant-Friedrichs-Lewy stability limit: Approach based on variable-length temporal and spatial operators

Hongyu Zhou, Yang Liu, Jing Wang

Research paper

Acoustic finite-difference modeling beyond conventional Courant-Friedrichs-Lewy stability limit: Approach based on variable-length temporal and spatial operators

Hongyu Zhou[1], Yang Liu[1,2,✉], and Jing Wang[1]

[1] *State Key Laboratory of Petroleum Resources and Prospecting*, *China University of Petroleum*, *Beijing* 102249, *China*
[2] *Karamay Campus China University of Petroleum* (*Beijing*), *Karamay* 834000, *China*

Corresponding author Liu Y, email: wliuyang@vip.sina.com

Key points:
- We have developed a new FD with variable-length temporal and spatial operators.
- The new FD simultaneously enhances the modeling stability and ensures the modeling accuracy.
- The new FD is more efficient than the conventional high-order FD method.

Abstract Conventional finite-difference (FD) methods cannot model acoustic wave propagation beyond Courant-Friedrichs-Lewy (CFL) numbers 0.707 and 0.577 for two-dimensional (2D) and three-dimensional (3D) equal spacing cases, respectively, thereby limiting time step selection. Based on the definition of temporal and spatial FD operators, we propose a variable-length temporal and spatial operator strategy to model wave propagation beyond those CFL numbers while preserving accuracy. First, to simulate wave propagation beyond the conventional CFL stability limit, the lengths of the temporal operators are modified to exceed the lengths of the spatial operators for high-velocity zones. Second, to preserve the modeling accuracy, the velocity-dependent lengths of the temporal and spatial operators are adaptively varied. The maximum CFL numbers for the proposed method can reach 1.25 and 1.0 in high velocity contrast 2D and 3D simulation examples, respectively. We demonstrate the effectiveness of our method by modeling wave propagation in simple and complex media.

Keywords: acoustic wave equation; finite-difference; stability condition; Courant-Friedrichs-Lewy numbers; variable length.

Citation: Zhou HY, Liu Y, and Wang J (2021). Acoustic finite-difference modeling beyond conventional Courant-Friedrichs-Lewy stability limit: Approach based on variable-length temporal and spatial operators. Earthq Sci **34**(2): 123–136, doi: 10.29382/eqs-2021-0009.

Received 30 March 2021; **received in revised form** 25 May 2021; **accepted** 27 May 2021; **available online** 11 June 2021.

1. Introduction

The finite-difference (FD) time-domain method has been applied extensively to solve wave equations for geophysical problems and provides a basis for seismic modeling (Alford et al., 1974; Kelly et al., 1976; Virieux, 1984; Dablain, 1986; Moczo et al., 2002; 2014; Yang DH et al., 2016) and imaging (Baysal et al., 1983; McMechan, 1983; Tarantola, 1984; Chen T and He BS, 2014; Du QZ et al., 2017; Qu YM et al., 2017). However, the stability of conventional FD methods, estimated by the Courant-Friedrichs-Lewy (CFL) number, imposes limitation on its use. For a specified velocity model and grid spacing, this limitation imposes a severe restriction on the maximum allowable time step for seismic modeling and imaging. The stability of FD modeling is often affected by the spatial and temporal accuracy.

Increasing spatial FD accuracy often deteriorates simulation stability (Fornberg, 1987; Liu Y and Sen MK, 2009a; Zhou HB and Zhang G, 2011; Zhang JH and Yao ZX, 2012; Wang EJ and Liu Y, 2018). Spatial discretization methods can be classified by the type of FD stencils, i.e., implicit or explicit. For wave equation simulation, spatial domain implicit FD stencils (Lele, 1992; Liu Y and Sen MK, 2009a, c) often exhibit worse stability than explicit ones (Dablain, 1986; Liu HF et al., 2014), although their accuracy is better. Depending on the method used to obtain FD coefficients, spatial FD approaches can be classified into two categories: Taylor-series expansion (TE) methods (Liu Y, 1998; Liu Y and Sen MK, 2009b, 2013) and optimization methods (Geller and Takeuchi, 1998; Zhang JH and Yao ZX, 2012; Liu Y, 2013). Between these methods, optimization methods achieve higher simulation accuracy than TE methods. Consequently, the simulation stability afforded by TE methods is better than that by optimization methods. Low-order spatial FD methods possess better stability than high-order ones, and the infinite order FD (pseudospectral) method exhibits the worst stability (Fornberg, 1987). Other combined FD methods using stencils and coefficients have been investigated. It has been demonstrated that modeling stability is inversely proportional to spatial accuracy (Wang EJ and Liu Y, 2018; Wang EJ et al., 2018; Xu SG and Liu Y, 2018).

Meanwhile, increasing temporal accuracy tends to improve simulation stability (Chen JB, 2007; Liu Y and Sen MK, 2013; Long GH et al., 2013; Wang EJ et al., 2016; Zhou HY et al., 2021). Lax-Wendroff (LW) schemes (Lax and Wendroff, 1960) are a typical class of effective methods. However, the exact high-order temporal accuracy of the LW method depends on the spectral accuracy of spatial derivatives (Long GH et al., 2013) and incurs a high computational cost. Alternative methods for enhancing stability include dispersion-relation-based FD methods by space (Dablain, 1986), time-space (Finkelstein and Kastner, 2007), and space-wavenumber domains (Song XL et al., 2013; Fomel et al., 2013; Fang G et al., 2014). Using the time-space domain method, Liu Y and Sen MK (2009b) enhanced FD modeling stability by achieving high-order temporal accuracy along eight acoustic wave propagation directions. To further improve the simulation stability, temporal accuracy was improved to a $(2N)$th-order accuracy along all propagation directions using a rhombus-shaped FD stencil (Liu Y and Sen MK, 2013), the maximum allowable CFL numbers of which were $\sqrt{2}/2 \approx 0.707$ and $\sqrt{3}/3 \approx 0.577$ for two-dimensional (2D) and three-dimensional (3D) equal spacing cases, respectively. To date, these CFL numbers remain the upper stability limit of the traditional temporal and spatial high-order time-space domain FD methods (Liu Y, 1998; Lines et al., 1999; Liu Y and Sen MK, 2009b; Wang EJ et al., 2016; Chen HM et al., 2016a, b; Ren ZM and Li ZC, 2017; Wang EJ and Liu Y, 2018). Practically, it is impossible to reach the CFL stability limit by balancing the modeling accuracy and stability using high-order or optimization methods.

In addition to increasing temporal and decreasing spatial accuracy, FD stability can be enhanced using perturbation methods (Li X et al., 2014; Gao YJ et al., 2018) by adjusting the eigenvalue of the time domain updating matrix. However, the FD updating process is memory and input/output (I/O) consuming, and this method cannot be applied easily to extremely large 2D models and moderate 3D models.

In this study, we aim to establish a stability enhancement FD modeling strategy using local stability and accuracy constraints. Our strategy is based on the analyses of the following two observations: First, increasing temporal accuracy and decreasing spatial accuracy can enhance modeling stability (Tan SR and Huang LJ, 2014; Wang EJ et al., 2016; Ren ZM et al., 2017; Ren ZM and Li ZC, 2017); second, high-velocity zones require stricter modeling stability than low-velocity zones. Therefore, the temporal and spatial operator lengths can be varied adaptively to ensure local modeling stability. In addition to stability, we incorporated the modeling accuracy constraint (Liu Y and Sen MK, 2011; Zhou HY et al., 2018) to ensure both aspects.

The remainder of this paper is organized as follows: First, we define the temporal and spatial operators and their lengths. Second, we propose the variable-length temporal and spatial operator (VLTSO) strategy, which can simultaneously enhance the modeling stability and maintain FD accuracy. Third, stability analyses and numerical examples to verify the features of the proposed VLTSO FD method are presented. Finally, our VLTSO FD method and conventional FD methods are compared; it is discovered that our stability-enhanced VLTSO FD method is more efficient when the same accuracy constraint is used.

2. Theory and method

2.1. Definition of temporal and spatial operators and their lengths

The constant density acoustic wave equation is expressed as

$$\frac{1}{v^2}\frac{\partial^2 p}{\partial t^2} = \Delta p, \tag{1}$$

where $p = p(x,z,t)$ and $p = p(x,y,z,t)$ are the wavefields for the 2D and 3D cases, respectively; $v = v(x,z)$ and $v = v(x,y,z)$ are the 2D and 3D velocity models, respectively; and Δ is the Laplace operator. Using rhombus- and octahedron-shaped operators (Liu Y and Sen MK, 2013; Xu SG and Liu Y, 2018), we define 2D and 3D temporal operators $\mathrm{D}_{\mathrm{t}}^{2N}$ as follows:

$$\frac{\partial^2 p}{\partial t^2} \approx \mathrm{D}_{\mathrm{t}}^{2N} p_{0,0}^0 = \frac{1}{\tau^2}(p_{0,0}^1 + p_{0,0}^{-1} - 2p_{0,0}^0) - \frac{v^2}{h^2}\left[\sum_{m=1}^{N-1}\sum_{n=1}^{N-m} a_{m,n}^{\mathrm{t}}\left(p_{-m,-n}^0 + p_{m,n}^0 + p_{-m,n}^0 + p_{m,-n}^0\right) + a_{0,0}^{\mathrm{t}} p_{0,0}^0 + \sum_{m=1}^{N} a_{m,0}^{\mathrm{t}}\left(p_{-m,0}^0 + p_{m,0}^0 + p_{0,m}^0 + p_{0,-m}^0\right)\right], \tag{2}$$

$$\frac{\partial^2 p}{\partial t^2} \approx \mathrm{D}_{\mathrm{t}}^{2N} p_{0,0,0}^0 = \frac{1}{\tau^2}(p_{0,0,0}^1 + p_{0,0,0}^{-1} - 2p_{0,0,0}^0) - \frac{v^2}{h^2} \times \left[\sum_{m=1}^{N-2}\sum_{n=1}^{N-m-1}\sum_{l=1}^{N-m-n} a_{m,n,l}^{\mathrm{t}} \begin{pmatrix} p_{m,n,l}^0 + p_{m,n,-l}^0 + p_{m,-n,l}^0 + p_{m,-n,-l}^0 \\ +p_{-m,n,l}^0 + p_{-m,n,-l}^0 + p_{-m,-n,l}^0 + p_{-m,-n,-l}^0 \end{pmatrix} + \sum_{m=1}^{N-1}\sum_{n=1}^{N-m} a_{m,n,0}^{\mathrm{t}} \begin{pmatrix} p_{-m,-n,0}^0 + p_{m,n,0}^0 + p_{-m,n,0}^0 + p_{m,-n,0}^0 + p_{-m,0,-n}^0 + p_{m,0,n}^0 \\ +p_{-m,0,n}^0 + p_{m,0,-n}^0 + p_{0,-m,-n}^0 + p_{0,m,n}^0 + p_{0,-m,n}^0 + p_{0,m,-n}^0 \end{pmatrix} + a_{0,0,0}^{\mathrm{t}} p_{0,0,0}^0 + \sum_{m=1}^{N} a_{m,0,0}^{\mathrm{t}}(p_{m,0,0}^0 + p_{-m,0,0}^0 + p_{0,m,0}^0 + p_{0,-m,0}^0 + p_{0,0,m}^0 + p_{0,0,-m}^0)\right], \tag{3}$$

where the discretized pressure wavefields are $p_{m,n}^o = p(x+mh, z+nh, t+o\tau)$ and $p_{m,n,l}^o = p(x+mh, y+nh, z+lh, t+o\tau)$ for the 2D and 3D cases, respectively; τ and h denote the time step and grid spacing, respectively; $a_{m,n}^{\mathrm{t}}$ and $a_{m,n,l}^{\mathrm{t}}$ are temporal derivative-related FD coefficients for the 2D and 3D cases, respectively. Using the TE method (Liu Y and Sen MK, 2013; Tan SR and Huang LJ, 2014), we can deduce the FD coefficients for $a_{m,n}^{\mathrm{t}}$ and $a_{m,n,l}^{\mathrm{t}}$. In the appendix, we present the derivation of these coefficients, which can be expressed as

$$\begin{cases} \sum_{m=1}^{N-1}\sum_{n=1}^{N-m} m^{2j-2\xi} n^{2\xi} a_{m,n}^{\mathrm{t}} = \dfrac{j!\, r^{2r-2}(2j-2\xi)!\,(2\xi)!}{2(2j)!\,\xi!\,(j-\xi)!} & \begin{pmatrix} \xi \in [1, \mathrm{int}(j/2)], \\ j \in [2, N] \end{pmatrix} \\ \sum_{m=1}^{N} m^2 a_{m,0}^{\mathrm{t}} + 2\sum_{m=1}^{N-1}\sum_{n=1}^{N-m} m^2 a_{m,n}^{\mathrm{t}} = 0 & \\ \sum_{m=1}^{N} m^{2j} a_{m,0}^{\mathrm{t}} + 2\sum_{m=1}^{N-1}\sum_{n=1}^{N-m} m^{2j} a_{m,n}^{\mathrm{t}} = r^{2j-2} & (j \in [2, N]) \\ a_{0,0}^{\mathrm{t}} + 4\sum_{m=1}^{N} a_{m,0}^{t} + 4\sum_{m=1}^{N-1}\sum_{n=1}^{N-m} a_{m,n}^{\mathrm{t}} = 0 & \end{cases}, \tag{4}$$

$$\begin{cases} \sum_{m=1}^{N-2}\sum_{n=1}^{N-m-1}\sum_{l=1}^{N-m-n} m^{2j-2\xi} n^{2\xi-2\psi} l^{2\psi} a_{m,n,l}^{\mathrm{t}} = \dfrac{j!\, r^{2j-2}(2j-2\xi)!(2\xi-2\psi)!(2\psi)!}{4(2j)!(j-\xi)!(\xi-\psi)!\psi!} & \begin{pmatrix} \psi \in [0, \mathrm{int}(j/3)], \\ \xi \in \left[2\psi, \mathrm{int}\left(\dfrac{j+\psi}{2}\right)\right] \end{pmatrix} \\ \sum_{m=1}^{N-1}\sum_{n=1}^{N-m} m^{2j-\xi} n^{2\xi} a_{m,n,0}^{\mathrm{t}} + 2\sum_{m=1}^{N-2}\sum_{n=1}^{N-m-1}\sum_{l=1}^{N-m-n} m^{2j-2\xi} n^{2\xi} a_{m,n,l}^{\mathrm{t}} = \dfrac{j!\, r^{2j-2}(2j-2\xi)!(2\xi)!}{2(2j)!(j-\xi)!} & \left(\xi \in \left[1, \mathrm{int}\left(\dfrac{j}{2}\right)\right]\right) \\ \sum_{m=1}^{N} m^2 a_{m,0,0}^{\mathrm{t}} + 4\sum_{m=1}^{N-1}\sum_{n=1}^{N-m} m^2 a_{m,n,0}^{\mathrm{t}} + 4\sum_{m=1}^{N-2}\sum_{n=1}^{N-m-1}\sum_{l=1}^{N-m-n} m^2 a_{m,n,l}^{\mathrm{t}} = 0 & \\ \sum_{m=1}^{N} m^{2j} a_{m,0,0}^{\mathrm{t}} + 4\sum_{m=1}^{N-1}\sum_{n=1}^{N-m} m^{2j} a_{m,n,0}^{\mathrm{t}} + 4\sum_{m=1}^{N-2}\sum_{n=1}^{N-m-1}\sum_{l=1}^{N-m-n} m^{2j} a_{m,n,l}^{\mathrm{t}} = r^{2j-2} & (j \in [2, N]) \\ a_{0,0,0}^{\mathrm{t}} + 6\sum_{m=1}^{N} a_{m,0,0}^{\mathrm{t}} + 12\sum_{m=1}^{N-1}\sum_{n=1}^{N-m} a_{m,n,0}^{\mathrm{t}} + 8\sum_{m=1}^{N-2}\sum_{n=1}^{N-m-1}\sum_{l=1}^{N-m-n} a_{m,n,l}^{\mathrm{t}} = 0 & \end{cases}, \tag{5}$$

where the CFL number is expressed as $r = v\tau/h$. To see the meaning of temporal operator, we convert Equations (2) and (3) into the frequency-wavenumber domain as follows:

$$-\omega^2 \approx -\omega^2 + 2\sum_{j=2}^{\infty} \frac{(-1)^j (kv)^{2j} \tau^{2j-2}}{(2j)!} - \frac{v^2}{h^2} \times \left[4\sum_{m=1}^{N-1}\sum_{n=1}^{N-m} a_{m,n}^{\mathrm{t}} \cos(mk_x h)\cos(nk_z h) + a_{0,0}^{\mathrm{t}} + 2\sum_{m=1}^{N} a_{m,0}^{\mathrm{t}}(\cos(mk_x h) + \cos(mk_z h))\right], \tag{6}$$

$$-\omega^2 \approx -\omega^2 + 2\sum_{j=2}^{\infty}\frac{(-1)^j (kv)^{2j}\tau^{2j-2}}{(2j)!} - \frac{v^2}{h^2}\times$$

$$\left\{8\sum_{m=1}^{N-2}\sum_{n=1}^{N-m-1}\sum_{l=1}^{N-m-n} a^{\mathrm{t}}_{m,n,l}\cos(mk_xh)\cos(nk_yh)\cos(lk_zh)+\right.$$

$$4\sum_{m=1}^{N-1}\sum_{n=1}^{N-m} a^{\mathrm{t}}_{m,n,0}[\cos(mk_xh)\cos(nk_yh)+\cos(mk_xh)\cos(nk_zh)+\cos(mk_yh)\cos(nk_zh)]+$$

$$\left. a^{\mathrm{t}}_{0,0,0} + 2\sum_{m=1}^{N} a^{\mathrm{t}}_{m,0,0}[\cos(mk_xh)+\cos(mk_yh)+\cos(mk_zh)]\right\}. \tag{7}$$

By using coefficients $a^{\mathrm{t}}_{m,n}$ and $a^{\mathrm{t}}_{m,n,l}$, the (2N)th-order temporal accuracy can be achieved by eliminating the high-order term τ^{2j-2} (j =1, 2, …, N) in Equations (6) and (7). Because N controls the order of the temporal accuracy, we define it as the temporal operator length. It is noteworthy that the temporal coefficients in Equations (4) and (5) are different from those of Liu Y and Sen MK (2013) and Xu SG and Liu Y (2018), since the coefficients presented herein contribute solely to the temporal accuracy, whereas the coefficients presented in the above-mentioned previous studies contribute to both temporal and spatial accuracies.

Using high-order FD, 2D and 3D spatial operators $\mathrm{D}_{\mathrm{s}}^{2M}$ can be defined as shown in Equations (8) and (9) for the 2D and 3D cases, respectively.

$$\Delta p \approx \mathrm{D}_{\mathrm{s}}^{2M} p_{0,0} = \frac{1}{h^2}\left[b^{\mathrm{s}}_{0,0}p^0_{0,0} + \sum_{m=1}^{M} b^{\mathrm{s}}_{m,0}(p^0_{m,0}+p^0_{-m,0}+p^0_{0,m}+p^0_{0,-m})\right], \tag{8}$$

$$\Delta p \approx \mathrm{D}_{\mathrm{s}}^{2M} p_{0,0,0} = \frac{1}{h^2}\left[b^{\mathrm{s}}_{0,0,0}p^0_{0,0,0} + \sum_{m=1}^{M} b^{\mathrm{s}}_{m,0,0}\begin{pmatrix} p^0_{m,0,0}+p^0_{-m,0,0}+p^0_{0,m,0} \\ +p^0_{0,-m,0}+p^0_{0,0,m}+p^0_{0,0,-m}\end{pmatrix}\right], \tag{9}$$

where $b^{\mathrm{s}}_{m,0}$ and $b^{\mathrm{s}}_{m,0,0}$ are spatial derivative-related FD coefficients (Liu Y, 1998), which are expressed as

$$\begin{cases} b^{\mathrm{s}}_{m,0,0} = b^{\mathrm{s}}_{m,0} = \dfrac{(-1)^{m+1}}{m^2}\prod\limits_{1\le i\le M, i\ne m}\left|\dfrac{i^2}{i^2-m^2}\right| (m=1,2,...,M) \\ b^{\mathrm{s}}_{0,0,0} = -6\sum\limits_{m=1}^{M} b^{\mathrm{s}}_{m,0,0}, b^{\mathrm{s}}_{0,0} = -4\sum\limits_{m=1}^{M} b^{\mathrm{s}}_{m,0} \end{cases}. \tag{10}$$

Because M controls the order of spatial accuracy, we define it as the spatial operator length. Based on the definition of the temporal and spatial operator lengths, we will discuss the method to control the modeling stability and accuracy in the following sections.

2.2. Stability criterion for conventional and proposed FD stencils

In this section, we derive the stability formulae for the conventional FD method (Lines et al., 1999) and proposed FD method using the eigenvalue method. By substituting Equations (2) and (8) into (1), the recursive form for the 2D case can be expressed as

$$p^1_{0,0} = \left(r^2\left(a^{\mathrm{t}}_{0,0}+b^{\mathrm{s}}_{0,0}\right)+2\right)p^0_{0,0} + r^2\left[\sum_{m=1}^{M} b^{\mathrm{s}}_{m,0}\left(p^0_{-m,0}+p^0_{m,0}+p^0_{0,m}+p^0_{0,-m}\right)\right]+$$

$$r^2\left[\sum_{m=1}^{N-1}\sum_{n=1}^{N-m} a^{\mathrm{t}}_{m,n}\left(p^0_{-m,-n}+p^0_{m,n}+p^0_{-m,n}+p^0_{m,-n}\right)+\sum_{m=1}^{N} a^{\mathrm{t}}_{m,0}\left(p^0_{-m,0}+p^0_{m,0}+p^0_{0,m}+p^0_{0,-m}\right)\right]-p^{-1}_{0,0}. \tag{11}$$

Converting Equation (11) into the wavenumber domain yields the following recursive matrix form:

$$\begin{pmatrix}\hat{p}^1_{0,0} \\ \hat{p}^0_{0,0}\end{pmatrix} = \begin{pmatrix} g & -1 \\ 1 & 0\end{pmatrix}\begin{pmatrix}\hat{p}^0_{0,0} \\ \hat{p}^{-1}_{0,0}\end{pmatrix}, \tag{12}$$

where

$$g = 2 + r^2\left(a^{\mathrm{t}}_{0,0} + b^{\mathrm{s}}_{0,0}\right) + 2r^2 \sum_{m=1}^{M} b^{\mathrm{s}}_{m,0}(\cos(mk_x h) + \cos(mk_z h)) +$$

$$2r^2 \sum_{m=1}^{N} a^{\mathrm{t}}_{m,0}(\cos(mk_x h) + \cos(mk_z h)) + 4r^2 \sum_{m=1}^{N-1}\sum_{n=1}^{N-m} a^{\mathrm{t}}_{m,n}(\cos(mk_x h)\cos(nk_z h)). \tag{13}$$

Here, $\hat{p}^k_{i,j}$ denotes the spatial Fourier transform of $p^k_{i,j}$. When $|g| \leqslant 2$, the eigenvalues of the transition matrix are within a unit circle and the simulation is stable (Liu Y and Sen MK, 2009b; 2013). Therefore,

$$r \leq \left[-\frac{a^{\mathrm{t}}_{0,0} + b^{\mathrm{s}}_{0,0}}{4} - \frac{1}{2}\sum_{m=1}^{M} b^{\mathrm{s}}_{m,0}(\cos(mk_x h) + \cos(mk_z h)) - \right.$$

$$\frac{1}{2}\sum_{m=1}^{N} a^{\mathrm{t}}_{m,0}(\cos(mk_x h) + \cos(mk_z h)) -$$

$$\left.\sum_{m=1}^{N-1}\sum_{n=1}^{N-m} a^{\mathrm{t}}_{m,n}(\cos(mk_x h)\cos(nk_z h))\right]^{-1/2}. \tag{14}$$

The FD simulation error generally increases with the wavenumber; therefore, we consider the Nyquist wavenumber $k_x = k_z = \pi/h$. Correspondingly, the stability condition of the 2D FD stencil is expressed as

$$r \leq s = \left[-\frac{a^{\mathrm{t}}_{0,0} + b^{\mathrm{s}}_{0,0}}{4} + \sum_{m=1}^{M} b^{\mathrm{s}}_{m,0}(-1)^{m-1} + \right.$$

$$\left.\sum_{m=1}^{N} a^{\mathrm{t}}_{m,0}(-1)^{m-1} + \sum_{m=1}^{N-1}\sum_{n=1}^{N-m} a^{\mathrm{t}}_{m,n}(-1)^{m+n-1}\right]^{-1/2}, \tag{15}$$

where s is the stability factor. As shown, s depends on M, N, $a^{\mathrm{t}}_{m,n}$, and $b^{\mathrm{s}}_{m,n}$. Moreover, $a^{\mathrm{t}}_{m,n}$ depends on parameters N and r, whereas $b^{\mathrm{s}}_{m,n}$ depends on M. For a model with fixed grid spacing h and time step τ, $r = v\tau/h$ is only affected by velocity v. Therefore, $s = s\ (M, N, v)$ is a function of M, N, and v.

When $N = 0$, Equation (15) is equivalent to the stability condition of the conventional FD stencil for 2D acoustic modeling, expressed as follows:

$$r \leq s = \left(-\frac{b^{\mathrm{s}}_{0,0}}{4} + \sum_{m=1}^{M} b^{\mathrm{s}}_{m,0}(-1)^{m-1}\right)^{-1/2}. \tag{16}$$

It is noteworthy that the stability factor s for the conventional FD in Equation (16) is only a function of a single parameter M, since $b^{\mathrm{s}}_{0,0}$ and $b^{\mathrm{s}}_{m,0}$ are functions of only M. It has been reported (Mitchell and Griffiths, 1980; Lines et al., 1999; Liu Y and Sen MK, 2009b) that the maximum allowable r for the conventional stencil is $r = \sqrt{2}/2 \approx 0.707 M = 1$. Furthermore, an increase in M deteriorates the modeling stability.

Using a similar method, we can prove the stability conditions of the conventional and proposed methods for the 3D case. The stability conditions are expressed as follows:

$$r \leq s(M) = \left(-\frac{b^{\mathrm{s}}_{0,0,0}}{4} + \frac{3}{2}\sum_{m=1}^{M} b^{\mathrm{s}}_{m,0,0}(-1)^{m-1}\right)^{-1/2}, \tag{17}$$

$$r \leq s(M,N,v) = \left[-\frac{a^{\mathrm{t}}_{0,0,0} + b^{\mathrm{s}}_{0,0,0}}{4} + \frac{3}{2}\sum_{m=1}^{M} b^{\mathrm{s}}_{m,0,0}(-1)^{m-1} + \right.$$

$$\frac{3}{2}\sum_{m=1}^{N} a^{\mathrm{t}}_{m,0,0}(-1)^{m-1} + 3\sum_{m=1}^{N-1}\sum_{n=1}^{N-m} a^{\mathrm{t}}_{m,n,0}(-1)^{m+n-1} + \tag{18}$$

$$\left. 2\sum_{m=1}^{N-2}\sum_{n=1}^{N-m-1}\sum_{l=1}^{N-m-n} a^{\mathrm{t}}_{m,n,l}(-1)^{m+n+l-1}\right]^{-1/2}.$$

The stability conditions shown in Equations (17) and (18) are those for the conventional method and proposed method, respectively. Analogously, the 3D stability condition for the conventional method (Lines et al., 1999) is a function of only M, whereas the stability condition for the proposed method is a function of M, N, and v. It has been reported (Mitchell and Griffiths, 1980; Lines et al., 1999; Liu Y and Sen MK, 2009b) that the best 3D modeling stability for the conventional method is $r \le \sqrt{3}/3 \approx 0.577$ with $M = 1$, and that an increase in M deteriorates the modeling stability.

2.3. Improving stability by modifying lengths of temporal and spatial operators

Conventional FD methods cannot stably model acoustic wave propagation when the CFL numbers exceed $\sqrt{2}/2 \approx 0.707$ and $\sqrt{3}/3 \approx 0.577$ for the 2D and 3D cases, respectively. In this section, we nullify this stability limit by modifying the length of the temporal operator N to exceed the length of the spatial operator M. Our modification is based on the observation that increasing temporal accuracy (increasing N) and decreasing spatial accuracy (decreasing M) can improve modeling stability (Liu Y and Sen MK, 2013; Tan SR and Huang LJ, 2014; Ren ZM and Li ZC, 2017). However, it has been reported (Liu Y and Sen MK, 2013; Wang EJ et al., 2016; Xu SG and Liu Y, 2018) that M is always designed to be greater than N. If we decrease M and increase N further until $M < N$, the stability may be further enhanced because the spatial and temporal accuracies are further decreased and increased, respectively. In this study, we investigate the case of $M < N$, which has never been tested previously. The stability analyses shown in Figures 1a and 1c show that when $M \ge N$, the maximum allowable CFL numbers do not exceed 0.707 and 0.577 for the 2D and 3D cases, respectively. However, Figures 1b and 1d show that with $M < N$ for our proposed method, the maximum allowable r increases significantly and overcomes the conventional stability limit. The numerical examples in Figure 2 verify that using the proposed method, 2D and 3D homogeneous acoustic wave propagations with r = 1.0, and 0.9 can be simulated, respectively, whereas most of conventional FD methods (Liu Y, 1998; Lines et al., 1999; Liu Y and Sen MK, 2013; Wang EJ et al., 2016) fail for such large r values.

2.4. Ensuring modeling accuracy based on variable-length temporal and spatial operators

For fixed-length operator modeling, stability is determined by the maximum velocity. The left half of snapshots from 2D and 3D two-layer examples presented in Figure 3 show that our stability-enhanced method [(M, N) = (2, 3)] guaranteed modeling stability. The maximum CFL numbers were 1.25 and 1.0 for the 2D and 3D cases, respectively, i.e., beyond the conventional CFL stability limit. However, a severe grid dispersion occurred. This is because such uniformed short operators cannot guarantee wave propagation accuracy in low-velocity zones. By increasing the operator length to (M, N) = (8, 6) and (8, 4) for the upper layers of the 2D and 3D models, respectively,

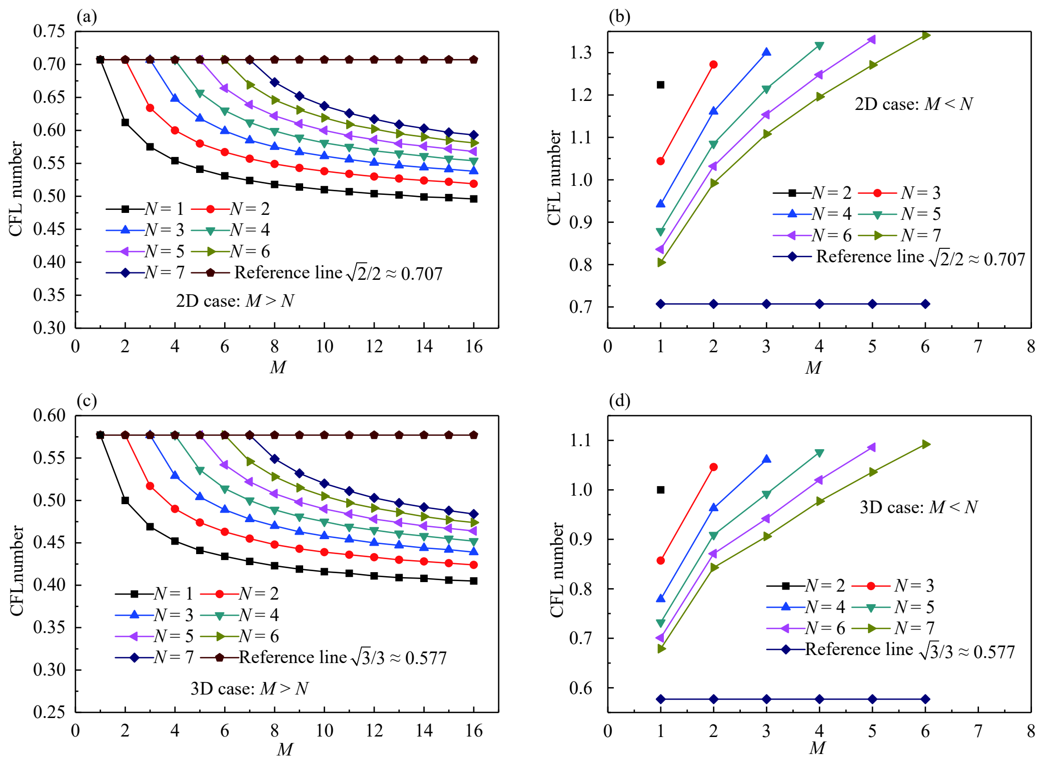

Figure 1. Stability curves of 2D (a and b) and 3D (c and d) cases. (a) and (c) show maximum allowable CFL numbers when $M > N$. (b) and (d) show maximum allowable CFL numbers when $M < N$.

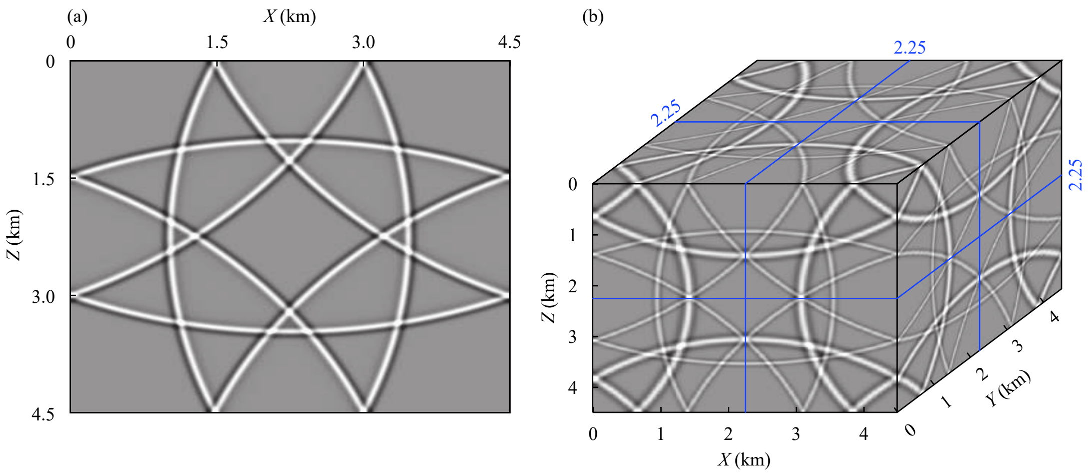

Figure 2. Snapshots of acoustic modeling beyond conventional CFL stability. v = 1500 m/s and h = 15 m. (a) 2D case with M = 5, N = 6, τ= 10 ms, and r = 1.0. (b) 3D case with M = 4, N = 5, τ= 9 ms, and r = 0.9. Source used was Ricker wavelet with 10 Hz peak frequency.

the modeling accuracy improved significantly, as shown in the right half of the snapshots in Figure 3. For a complex geology model, however, manually adjustment (M, N) is impractical; therefore, we propose an adaptive VLTSO strategy to guarantee the modeling accuracy of the proposed stability enhancement method.

For a specified time step and grid spacing, the modeling error can be expressed as follows:

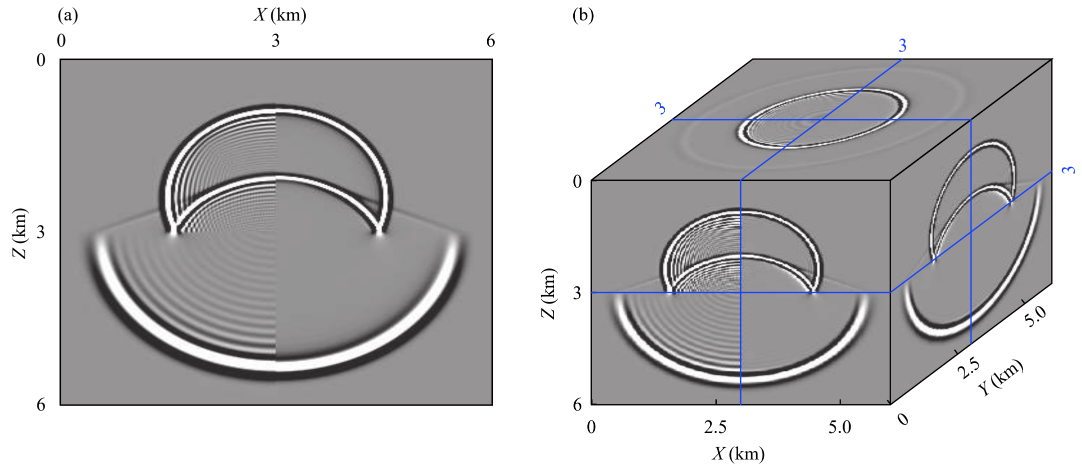

Figure 3. Fixed and variable (M, N) modeling for two-layer models. (a) Maximum r = 1.25. (b) Maximum r = 1.0. Velocities of upper and lower layers were 2000 and 5000 m/s, respectively; interface at z = 3000 m, and grid spacing was h = 20 m. Left half of 2D (a) and 3D (b) snapshots were simulated with fixed (M, N), whereas right half with variable (M, N). Source used was Ricker wavelet with 15 Hz peak frequency.

$$\varepsilon_{\max}(M,N,v,f_{\max}) = \max\{|\varepsilon(M,N,v,f)|\},\ f\in[0,f_{\max}], \tag{19}$$

where max is the largest value of a function, and $\varepsilon(M,N,v,f) = h/v_{\rm FD} - h/v = h(\delta^{-1}-1)/v$ denotes the spatial grid propagation time error (Liu Y and Sen MK, 2011). $v_{\rm FD}$ denotes the numerical velocity, δ is expressed as $\delta = v_{\rm FD}/v$, and $f_{\max}$ is the maximum modeling frequency. The expression for the stability factor s (M, N, v) is presented in Equations (15) and (18) for the 2D and 3D cases, respectively. We set the local modeling accuracy and stability constraints to the following:

$$\varepsilon_{\max}(M,N,v,f_{\max}) < \eta, \tag{20}$$

$$r < s(M,N,v), \tag{21}$$

where η is the maximum allowable modeling error. For fixed values of v and $f_{\max}$, $\varepsilon_{\max}$ and s are related to only M and N. Therefore, we aim to identify local M and N values that satisfy the accuracy and stability constraints in both Equations (20) and (21).

Directly identifying M and N for each velocity is a time-consuming 2D problem. Hence, we converted the 2D search problem into two one-dimensional problems. It has been reported that when $M = N$, spatial dispersion is dominant (Liu Y and Sen MK, 2013). Therefore, we can identify an M value that satisfies the spatial accuracy by setting $M = N$ first, followed by fixing the M identified and then obtaining an N value from $[1, M]$ that satisfies stability and temporal accuracies. Exceptions occur when $r > \sqrt{2}/2$ (2D) and $\sqrt{3}/3$ (3D), in which case N must be increased slightly such that $N > M$ to ensure modeling stability beyond the conventional limit. The detailed procedures are as follows:

Step 1. For each velocity value, set $M = N = M_{max}$ first and then gradually decrease M to a minimum value M_{min} that satisfies the accuracy constraint shown in Equation (20).

Step 2. If $r < \sqrt{2}/2$ and $\sqrt{3}/3$ for the 2D and 3D cases, respectively, then gradually decrease N from $N = M_{min}$ to a minimum value N_{min} that satisfies the accuracy and stability constraints shown in Equations (20) and (21). Otherwise, gradually increase N from $N = M_{min}$ to an effective value N_{min} that satisfies the stability condition shown in Equation (21).

Step 3. Identify M_{min} and N_{min} to perform wave extrapolation for the velocity.

The operator length variation shown in Figure 3 was determined using our VLTSO strategy with a small error constraint $\eta = 10^{-5}$ and $f_{max} = 30$ Hz. We compare the VLTSO traces with the reference solution shown in Figure 7a and discovered that the VLTSO strategy can guarantee the modeling accuracy of the stability-enhanced method, including in high velocity contrast media.

3. Numerical examples

In this section, we verfiy the stability enhanced and accuracy preserving properties of our VLTSO FD strategy using complex 2D and 3D Society of Exploration Geophysicists/European Association of Geoscientists and Engineers (SEG/EAGE) (Aminzadeh et al., 1996) salt models (Figure 4a). The 2D model is a slice of the 3D model at $x = 6.76$ km.

The temporal and spatial operator lengths of the 2D and 3D models were automatically determined based on the VLTSO strategy, as shown in Figure 5. We observe that the temporal operator was longer than the spatial operator in high-velocity zones, thereby ensuring modeling with maximum CFL numbers of 0.8966 and 0.67245 for the 2D and 3D cases, respectively, which surpassed the conventional stability limits. Figure 6 shows the seismic records of the 2D and 3D modeling cases. The Ricker source with a 10 Hz peak frequency was located at $(x, z) = (3.38, 0.2)$ km for the 2D case, and $(x, y, z) = (3.38, 3.38, 0.2)$ km for the 3D case. The receivers were placed evenly with an interval of 20 m at depth $z = 0.2$ km. The duration of the seismic record was 6.0 s. The 2D and 3D seismic records shown in Figure 6 and the 3D snapshot in Figure 4b validated the stable modeling. In addition, our wavefield snapshot and seismic records did not indicate clear grid dispersions because the accuracy was guaranteed by the operator length variation with a small error constraint. The trace comparison between the VLTSO method and the reference method, generated by a long spatial operator ($M = 32$) plus the time dispersion removal method (Koene et al., 2017), further demonstrates the accuracy preserving property of our method, as shown in Figure 7b.

4. Discussion

In this section, we discuss the computational cost, memory, and I/O usage of our proposed VLTSO method. First, we compare the computational cost of our VLTSO FD method with that of a conventional FD method (Liu Y, 1998; Lines et al., 1999) for acoustic wave modeling.

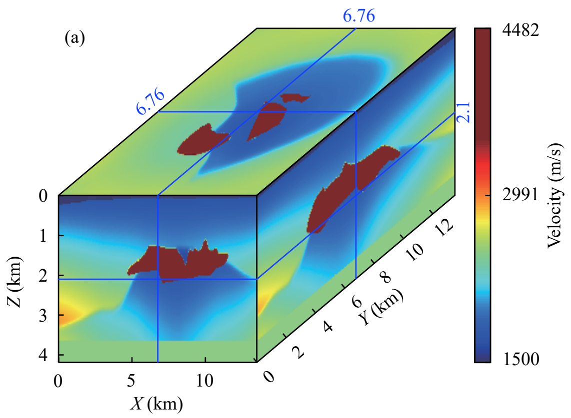

Figure 4. (a) SEG/EAGE 3D model with grid spacing $h = 20$ m. (b) Wavefield snapshot with r of 0.67245. Source used was Ricker wavelet, with 10 Hz peak frequency, located at $(x, y, z) = (3.38, 3.38, 0.2)$ km.

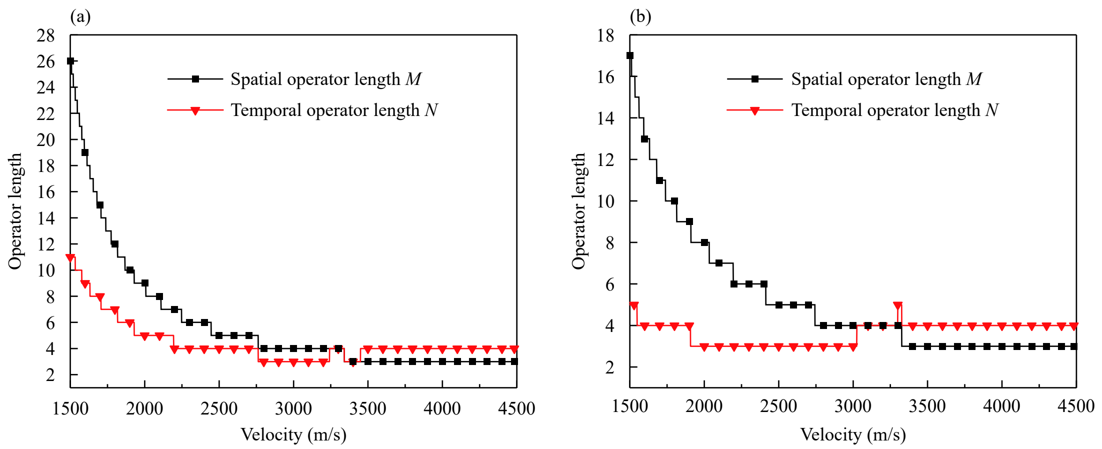

Figure 5. 2D (a) and 3D (b) operator length variation by VLTSO strategy for stability-enhanced method. Time steps were 4 and 3 ms for 2D and 3D cases, respectively. $\eta = 10^{-5}$ and $f_{\max} = 30$ Hz.

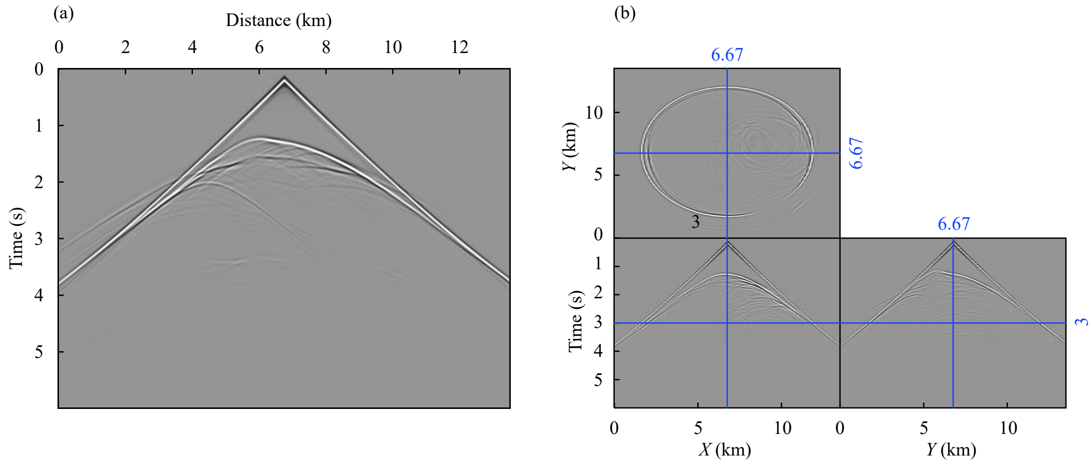

Figure 6. 2D (a) and 3D (b) seismic records with maximum r values of 0.8966 and 0.67245, respectively.

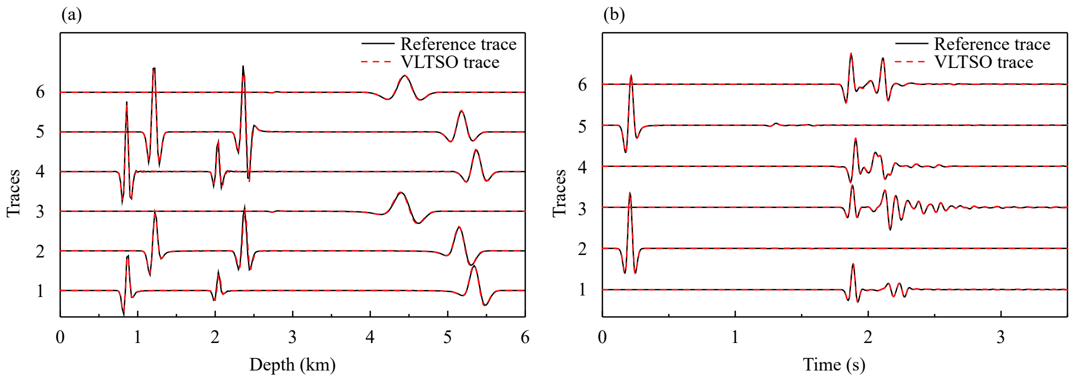

Figure 7. Trace comparison between variable length and reference solution. (a) Traces from 2D (trace 1 at $x = 3.0$ km, trace 2 at $x = 4.0$ km, and trace 3 at $x = 5.0$ km) and 3D (trace 4 at $(x, y) = (3.0, 3.0)$ km, trace 5 at $(x, y) = (3.0, 4.0)$ km, and trace 6 at $(x, y) = (3.0, 5.0)$ km) high velocity contrast modeling shown in Figure 3. (b) Traces from 2D (trace 1 at $x = 3.76$ km, trace 2 at $x = 6.76$ km, and trace 3 at $x = 9.76$ km) and 3D (trace 4 at $(x, y) = (6.76, 3.76)$ km, trace 5 at $(x, y) = (6.76, 6.76)$ km, and trace 6 at $(x, y) = (6.76, 9.76)$ km) seismic records shown in Figure 6.

Consider the 2D SEG/EAGE model as an example, where the grid spacing is 20 m, and the maximum velocity is 4483 m/s. The conventional method cannot stably model the wave propagation beyond $r = \sqrt{2}/2 \approx 0.707$, which is equivalent to a time step of $\tau = 3$ ms. To adopt the time step, the spatial operator length $M = 1$ (second-order spatial accuracy) can be used. The modeling accuracy may not be ensured by such low-order FDs, as indicated in

Figure 8a. To reach a modeling accuracy comparable to that of the VLTSO method, M must be increased. However, an increase in M deteriorates the modeling stability (Liu Y, 1998; Lines et al., 1999), which necessitates a reduction in the time step. When using the error constraints in Equation (20) (which are the same as that of the VLTSO method), M = 26 and time step τ = 0.7 ms must be adopted in the conventional FD method. The snapshots shown in Figures 8b and 8c demonstrate that using these parameters, the conventional FD method can achieve an accuracy comparable to that of the VLTSO FD method. Based on a similar accuracy, we compare the CPU times for the two methods, as shown in Figure 9a; it was revealed that compared with the conventional FD method, our VLTSO FD method significantly reduced the computational cost. Using the same approach, we present the 3D graphic processing unit (GPU) times for the two methods in Figure 9b, in which a conclusion similar to that of the 2D case is obtained. It is noteworthy that we used the same CPU (Intel Xeon CPU E5-2640) and GPU (Tesla K40c) devices for timing the conventional and VLTSO FD methods. Next, we discuss the memory usage of the VLTSO method. Compared with the conventional FD method, the VLTSO method involves identical spatial operators for the FD coefficients. Therefore, the same amount of memory is used to store the spatial FD coefficients in the VLTSO method. The only difference is the additional storage requirement for the FD coefficients of the temporal operator. The temporal FD coefficients in Equations (4) and (5) are related to r or velocity, and we can calculate and store the coefficients for representative velocities with a small interval, such as 1 m/s. For the VLTSO method, only 119 and 149 kB of memory are required to store the FD coefficients for the 2D and 3D cases when $v \in [1500, 4483]$ m/s, respectively. The additional memory cost is low and acceptable. Finally, we discuss the I/O usage of the VLTSO method. Similar to the conventional FD method, the proposed VLTSO method only requires local communication rather than global communication such as the pseudospectra method. Therefore, our VLTSO method can be accelerated using a GPU device.

5. Conclusions

In this study, we develope a VLTSO FD strategy that can model wave propagation beyond the conventional CFL

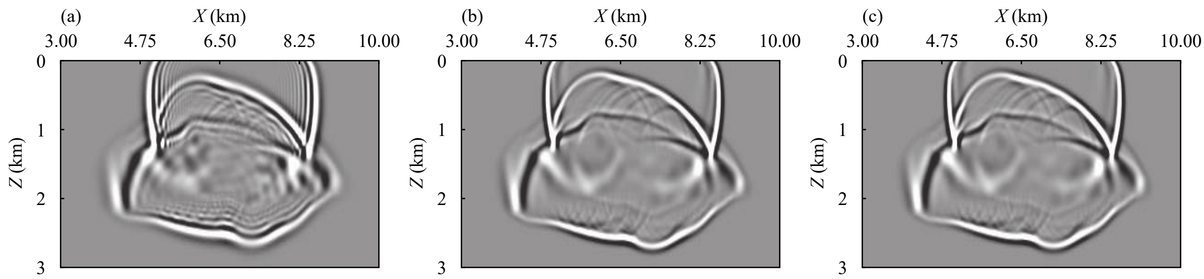

Figure 8. Snapshots at 1.26 s generated by conventional FD method with M = 1 and time step 3 ms (a); conventional FD method with M = 26 and time step 0.7 ms (b); new VLTSO method with time step 4 ms, and operator lengths are shown in Figure 5a (c).

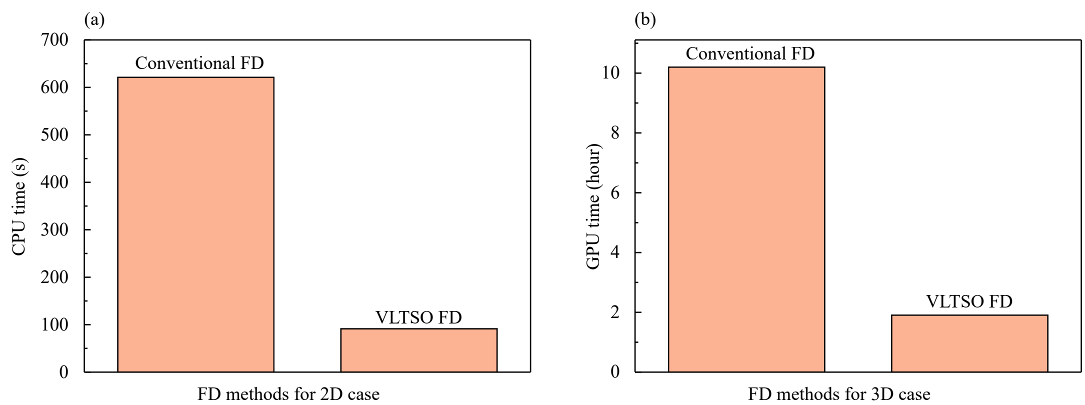

Figure 9. Computational cost analyses of two FD methods using same accuracy constraints. Recording time was 6.0 s. (a) CPU time of 2D salt model simulation for conventional FD and VLTSO FD methods; (b) GPU time of 3D salt model simulation for conventional FD and VLTSO FD methods.

stability limit while preserving accuracy. The controlled temporal and spatial operator lengths for the high-velocity area guaranteed modeling stability, whereas the adaptive operator length variations guaranteed the modeling accuracy and efficiency for other areas. Because of the enhanced stability, our proposed method can adopt a larger time step than the conventional FD method when using the same grid spacing and velocity model. For the same accuracy demand, our VLTSO FD method is more efficient than the conventional high-order FD method. The stability analyses, modeling examples, and comparisons of the computational costs between our method and the conventional FD method validated the effectiveness of the proposed VLTSO FD strategy.

Acknowledgements:

This work was supported by the National Natural Science Foundation of China (No.41874144) and by the Research Foundation of China University of Petroleum-Beijing at Karamay (RCYJ2018A-01-001).

Appendix: FD coefficients for temporal operator

In this appendix, we deduce the FD coefficients for the 2D and 3D temporal operators using the TE method.

First, we provide the derivation of the FD coefficients for the 2D case and elucidate how these coefficients afford (2N)th-order temporal accuracy. First, we present the conventional center FD for the temporal derivative, as follows:

$$\frac{\partial^2 p}{\partial t^2} \approx \frac{1}{\tau^2}(p_{0,0}^1 + p_{0,0}^{-1} - 2p_{0,0}^0). \quad (A1)$$

Transforming Equation (2) into the frequency-wavenumber domain yields

$$-\omega^2 \approx \frac{-2+2\cos(\omega\tau)}{\tau^2}. \quad (A2)$$

Applying TE to the trigonometric functions yields

$$-\omega^2 \approx 2\sum_{j=1}^{\infty}\frac{(-1)^j(\omega\tau)^{2j}}{(2j)!\tau^2} = -\omega^2 + 2\sum_{j=2}^{\infty}\frac{(-1)^j(\omega\tau)^{2j}}{(2j)!\tau^2}. \quad (A3)$$

Comparing both sides of Equation (A3), it is observed that $2\sum_{j=2}^{\infty}\frac{(-1)^j(\omega\tau)^{2j}}{(2j)!\tau^2}$ is the error term. Because the minimum power of τ in the error term is two, the accuracy of the conventional center FD is of the second order. To increase the temporal accuracy to the (2N)th-order, we must eliminate the high-order terms $\frac{2(-1)^j(\omega\tau)^{2j}}{(2j)!\tau^2}$ (j =2, 3, …, N) in Equation (A3). Using the dispersion relation $\omega = kv$ and binomial theorem

$$k^{2j} = (k_x^2 + k_z^2)^j = \sum_{\varepsilon=0}^{j}\frac{j!}{(j-\varepsilon)!\varepsilon!}k_x^{2(j-\varepsilon)}k_z^{2\varepsilon}, \quad (A4)$$

we have

$$\frac{2(-1)^j(\omega\tau)^{2j}}{(2j)!\tau^2} = \frac{2(-1)^j(kv\tau)^{2j}}{(2j)!\tau^2} = \frac{2(-1)^j(v\tau)^{2j}}{(2j)!\tau^2}\sum_{\varepsilon=0}^{j}\frac{j!}{(j-\varepsilon)!\varepsilon!}k_x^{2(j-\varepsilon)}k_z^{2\varepsilon}. \quad (A5)$$

Therefore, eliminating the term $\frac{2(-1)^j(\omega\tau)^{2j}}{(2j)!\tau^2}$ (j =2, 3, …, N) is equivalent to eliminating $\frac{2(-1)^j(v\tau)^{2j}}{(2j)!\tau^2}\sum_{\varepsilon=0}^{j}\frac{j!}{(j-\varepsilon)!\varepsilon!}k_x^{2(j-\varepsilon)}k_z^{2\varepsilon}$ (j =2, 3, …, N). Next, we prove that this can be achieved using Equation (2). By transforming Equation (2) into the frequency-wavenumber domain, we obtain

$$-\omega^2 \approx \frac{-2+2\cos(\omega\tau)}{\tau^2} - \frac{v^2}{h^2}\left[\begin{array}{l} 4\sum_{m=1}^{N-1}\sum_{n=1}^{N-m}a_{m,n}^{\mathrm{t}}\cos(mk_xh)\cos(nk_zh) + \\ a_{0,0}^{\mathrm{t}} + 2\sum_{m=1}^{N}a_{m,0}^{\mathrm{t}}(\cos(mk_xh)+\cos(mk_zh)) \end{array}\right]. \quad (A6)$$

Applying TE to the trigonometrical functions and using Equation (A5), we obtain

$$2\sum_{j=2}^{\infty}\frac{(-1)^j(v\tau)^{2j}}{(2j)!\tau^2}\sum_{\varepsilon=0}^{j}\frac{j!}{(j-\varepsilon)!\varepsilon!}k_x^{2(j-\varepsilon)}k_z^{2\varepsilon} \approx \frac{v^2}{h^2}\left[\begin{array}{l} 4\sum_{m=1}^{N-1}\sum_{n=1}^{N-m}a_{m,n}^{\mathrm{t}}\sum_{\varepsilon=0}^{\infty}\sum_{\xi=0}^{\infty}\frac{(-1)^{\varepsilon+\xi}m^{2\varepsilon}n^{2\xi}h^{2(\varepsilon+\xi)}}{(2\varepsilon)!(2\xi)!}{k_x}^{2\varepsilon}{k_z}^{2\xi} \\ +a_{0,0}^{\mathrm{t}} + 2\sum_{m=1}^{N}a_{m,0}^{\mathrm{t}}\sum_{j=0}^{\infty}\frac{(-1)^j m^{2j}h^{2j}}{(2j)!}\left(k_x^{2j}+k_z^{2j}\right) \end{array}\right]. \quad (A7)$$

It is noteworthy that $\frac{2(-1)^j(v\tau)^{2j}}{(2j)!\tau^2}\sum_{\varepsilon=0}^{j}\frac{j!}{(j-\varepsilon)!\varepsilon!}k_x^{2(j-\varepsilon)}k_z^{2\varepsilon}$ can be decomposed into components that include ${k_x}^{2\varepsilon}{k_z}^{2\xi}$, ${k_x}^{2j}$, ${k_z}^{2j}$, and zero wavenumbers. We can eliminate $\frac{2(-1)^j(v\tau)^{2j}}{(2j)!\tau^2}\sum_{\varepsilon=0}^{j}\frac{j!}{(j-\varepsilon)!\varepsilon!}k_x^{2(j-\varepsilon)}k_z^{2\varepsilon}$ by counteracting each component with the terms on the right side of Equation (A7). Comparing the terms ${k_x}^{2\varepsilon}{k_z}^{2\xi}(\varepsilon+\xi = j,\ \varepsilon \neq 0,\ \xi \neq 0\ )$ on both sides of Equation (A7) yields

$$4\sum_{m=1}^{N-1}\sum_{n=1}^{N-m} a_{m,n}^{\mathrm{t}} \frac{(-1)^j m^{2(j-\varepsilon)} n^{2\varepsilon} h^{2(j-1)}}{(2(j-\varepsilon))!(2\varepsilon)!} = 2\frac{(-1)^j j!(v\tau)^{2j-2}}{(2j)!(j-\varepsilon)!\varepsilon!}. \tag{A8}$$

Comparing the terms ${k_x}^{2j}$ or ${k_z}^{2j}$ on both sides of Equation (A7) yields

$$4\sum_{m=1}^{N-1}\sum_{n=1}^{N-m} a_{m,n}^{\mathrm{t}} m^2 + 2\sum_{m=1}^{M} a_{m,0}^{\mathrm{t}} m^2 = 0, \tag{A9}$$

$$4\sum_{m=1}^{N-1}\sum_{n=1}^{N-m} a_{m,n}^{\mathrm{t}} \frac{(-1)^j m^{2j} h^{2(j-1)}}{(2j)!} + 2\sum_{m=1}^{M} a_{m,0}^{\mathrm{t}} \frac{(-1)^j m^{2j} h^{2(j-1)}}{(2j)!} = 2\frac{(-1)^j (v\tau)^{2j-2}}{(2j)!}. \tag{A10}$$

Comparing the zero wavenumber components on both sides of Equation (A7) yields

$$4\sum_{m=1}^{N-1}\sum_{n=1}^{N-m} a_{m,n}^{\mathrm{t}} + a_{0,0}^{\mathrm{t}} + 4\sum_{m=1}^{M} a_{m,0}^{\mathrm{t}} = 0. \tag{A11}$$

By grouping the independent equations shown in Equations (A8), (A9), (A10), and (A11) and rearranging them, we arrive at Equation (4), which is the expression of 2D FD coefficients for the temporal operator. Because high-order terms $\frac{2(-1)^j(\omega\tau)^{2j}}{(2j)!\tau^2} (j \le N)$ can be counteracted by Equation (4), the (*2N*)th-order temporal accuracy can be obtained.

Next, we provide the derivation of the FD coefficients for the 3D case. The idea and workflow are similar to those of the 2D case. By transforming Equation (3) into the frequency–wavenumber domain, we obtain

$$-\omega^2 \approx \frac{2\cos(\omega\tau)-2}{\tau^2} - \frac{v^2}{h^2}\cdot \left\{ \begin{array}{l} 8\sum\limits_{m=1}^{N-2}\sum\limits_{n=1}^{N-m-1}\sum\limits_{l=1}^{N-m-n} a_{m,n,l}^{\mathrm{t}} \cos(mk_xh)\cos(nk_yh)\cos(lk_zh)+ \\ 4\sum\limits_{m=1}^{N-1}\sum\limits_{n=1}^{N-m} a_{m,n,0}^{\mathrm{t}} [\cos(mk_xh)\cos(nk_yh)+\cos(mk_xh)\cos(nk_zh)+\cos(mk_yh)\cos(nk_zh)]+ \\ a_{0,0,0}^{\mathrm{t}} + 2\sum\limits_{m=1}^{N} a_{m,0,0}^{\mathrm{t}} [\cos(mk_xh)+\cos(mk_yh)+\cos(mk_zh)] \end{array} \right\}. \tag{A12}$$

Applying TE for the trigonometric functions and $\omega = kv$, we obtain

$$2\sum_{j=2}^{\infty} \frac{(-1)^j (kv\tau)^{2j}}{(2j)!\tau^2} \approx \frac{v^2}{h^2} \times \left\{ \begin{array}{l} 8\sum\limits_{m=1}^{N-2}\sum\limits_{n=1}^{N-m-1}\sum\limits_{l=1}^{N-m-n} a_{m,n,l}^{\mathrm{t}} \sum\limits_{\varepsilon=0}^{\infty}\sum\limits_{\xi=0}^{\infty}\sum\limits_{\psi=0}^{\infty} \frac{(-1)^{\varepsilon+\xi+\psi} m^{2\varepsilon} n^{2\xi} l^{2\psi} h^{2(\varepsilon+\xi+\psi)}}{(2\varepsilon)!(2\xi)!(2\psi)!} {k_x}^{2\varepsilon}{k_y}^{2\xi}{k_z}^{2\psi}+ \\ 4\sum\limits_{m=1}^{N-1}\sum\limits_{n=1}^{N-m} a_{m,n,0}^{\mathrm{t}} \sum\limits_{\varepsilon=0}^{\infty}\sum\limits_{\xi=0}^{\infty} \frac{(-1)^{\varepsilon+\xi} m^{2\varepsilon} n^{2\xi} h^{2(\varepsilon+\xi)}}{(2\varepsilon)!(2\xi)!} \left({k_x}^{2\varepsilon}{k_y}^{2\xi} + {k_x}^{2\varepsilon}{k_z}^{2\xi} + {k_y}^{2\varepsilon}{k_z}^{2\xi}\right)+ \\ a_{0,0,0}^{\mathrm{t}} + 2\sum\limits_{m=1}^{N} a_{m,0,0}^{\mathrm{t}} \sum\limits_{j=0}^{\infty} \frac{(-1)^j m^{2j} h^{2j}}{(2j)!} \left(k_x^{2j}+k_y^{2j}+k_z^{2j}\right) \end{array} \right\}. \tag{A13}$$

Using the trinomial theorem, we obtain

$$k^{2j} = (k_x^2+k_y^2+k_z^2)^j = \sum_{\varepsilon=0}^{j}\sum_{\xi=0}^{\varepsilon} \frac{j!}{(j-\varepsilon)!(\varepsilon-\xi)!\xi!} k_x^{2(j-\varepsilon)} k_y^{2(\varepsilon-\xi)} k_z^{2\xi}. \tag{A14}$$

Substituting Equation (A14) into Equation (A13) and comparing the terms ${k_x}^{2\varepsilon}{k_y}^{2\xi}{k_z}^{2\psi}$ ($\varepsilon+\xi+\psi = j$, $\varepsilon \ne 0$, $\xi \ne 0$ and $\psi \ne 0$) on both sides of Equation (A13) yields

$$8\sum_{m=1}^{N-2}\sum_{n=1}^{N-m-1}\sum_{l=1}^{N-m-n} a_{m,n,l}^{\mathrm{t}} \frac{(-1)^j m^{2(j-\varepsilon)} n^{2(\varepsilon-\xi)} l^{2\xi} h^{2(j-1)}}{(2(j-\varepsilon))!(2(\varepsilon-\xi))!(2\xi)!} = 2\frac{(-1)^j j!(v\tau)^{2j-2}}{(2j)!(j-\varepsilon)!(\varepsilon-\xi)!\xi!}. \tag{A15}$$

Comparing terms ${k_x}^{2\varepsilon}{k_y}^{2\xi}$, ${k_x}^{2\varepsilon}{k_z}^{2\xi}$, or ${k_y}^{2\varepsilon}{k_z}^{2\xi}$($\varepsilon+\xi = j, \varepsilon \ne 0, \xi \ne 0$) on both sides of Equation (A13) yields

$$8\sum_{m=1}^{N-2}\sum_{n=1}^{N-m-1}\sum_{l=1}^{N-m-n} a_{m,n,l}^{\mathrm{t}} \frac{(-1)^j m^{2(j-\varepsilon)} n^{2\varepsilon} h^{2(j-1)}}{(2(j-\varepsilon))!(2\varepsilon)!} + 4\sum_{m=1}^{N-1}\sum_{n=1}^{N-m} a_{m,n,0}^{\mathrm{t}} \frac{(-1)^j m^{2(j-\varepsilon)} n^{2\varepsilon} h^{2(j-1)}}{(2(j-\varepsilon))!(2\varepsilon)!} = 2\frac{(-1)^j j!(v\tau)^{2j-2}}{(2j)!(j-\varepsilon)!\varepsilon!}. \tag{A16}$$

Comparing terms ${k_x}^{2j}$, ${k_y}^{2j}$, or ${k_z}^{2j}$ on both sides of Equation (A13) yields

$$8\sum_{m=1}^{N-2}\sum_{n=1}^{N-m-1}\sum_{l=1}^{N-m-n}a^{\mathrm{t}}_{m,n,l}m^2+8\sum_{m=1}^{N-1}\sum_{n=1}^{N-m}a^{\mathrm{t}}_{m,n,0}m^2+2\sum_{m=1}^{M}a^{\mathrm{t}}_{m,0,0}m^2=0, \tag{A17}$$

$$\begin{aligned}&8\sum_{m=1}^{N-2}\sum_{n=1}^{N-m-1}\sum_{l=1}^{N-m-n}a^{\mathrm{t}}_{m,n,l}\frac{(-1)^j m^{2j}h^{2(j-1)}}{(2j)!}+8\sum_{m=1}^{N-1}\sum_{n=1}^{N-m}a^{\mathrm{t}}_{m,n,0}\frac{(-1)^j m^{2j}h^{2(j-1)}}{(2j)!}+\\&2\sum_{m=1}^{M}a^{\mathrm{t}}_{m,0,0}\frac{(-1)^j m^{2j}h^{2(j-1)}}{(2j)!}=2\frac{(-1)^j(v\tau)^{2j-2}}{(2j)!}.\end{aligned} \tag{A18}$$

Comparing the zero wavenumber components on both sides of Equation (A13) yields

$$\begin{aligned}&8\sum_{m=1}^{N-2}\sum_{n=1}^{N-m-1}\sum_{l=1}^{N-m-n}a^{\mathrm{t}}_{m,n,l}+12\sum_{m=1}^{N-1}\sum_{n=1}^{N-m}a^{\mathrm{t}}_{m,n,0}+\\&a^{\mathrm{t}}_{0,0,0}+6\sum_{m=1}^{M}a^{\mathrm{t}}_{m,0,0}=0.\end{aligned} \tag{A19}$$

By grouping the independent equations shown in Equations (A15), (A16), (A17), (A18), and (A19) and rearranging them, we obtain Equation (5), which yields the 3D FD coefficients for the temporal operator.

References

Alford R, Kelly K, and Boore DM (1974). Accuracy of finite-difference modeling of the acoustic wave equation. Geophysics **39**: 834–842.

Aminzadeh F, Burkhard N, Long J, Kunz T, and Duclos P (1996) Three dimensional SEG/EAEG models — An update. The Leading Edge 15: 131-134.

Baysal E, Kosloff DD, and Sherwood JW (1983). Reverse time migration. Geophysics **48**: 1 514–1 524.

Chen HM, Zhou H, Zhang QC and Chen Y (2016a). Modeling elastic wave propagation using k-space operator-based temporal high-order staggered-grid finite-difference method. IEEE Transactions on Geoscience and Remote Sensing **55**: 801–815.

Chen HM, Zhou H, Zhang QC, Xia MM and Li QQ (2016b). A k-space operator-based least-squares staggered-grid finite-difference method for modeling scalar wave propagation. Geophysics **81**: T45–T61.

Chen T, and He BS (2014). A normalized wave field separation cross-correlation imaging condition for reverse time migration based on Poynting vector. Applied Geophysics **11**: 158–166.

Chen JB (2007). High-order time discretizations in seismic modeling. Geophysics **72**: SM115–SM122.

Dablain M (1986). The application of high-order differencing to the scalar wave equation. Geophysics **51**(1): 54–66.

Du QZ, Guo CF, Zhao Q, Gong XF, Wang CX and Li XY (2017). Vector-based elastic reverse time migration based on scalar imaging condition. Geophysics **82**(2): S111–S127.

Fang G, Fomel S, Du QZ, and Hu JW (2014). Lowrank seismic-wave extrapolation on a staggered grid. Geophysics **79**(3): T157–T168.

Finkelstein B, and Kastner R (2007). Finite difference time domain dispersion reduction schemes. Journal of Computational Physics **221 (1)**: 422–438.

Fomel S, Ying LX, and Song XL (2013). Seismic wave extrapolation using lowrank symbol approximation. Geophysical Prospecting **61**(3): 526–536.

Fornberg B (1987). The pseudospectral method: Comparisons with finite differences for the elastic wave equation. Geophysics **52**: 483–501.

Gao YJ, Zhang JH, and Yao ZX (2018). Removing the stability limit of the explicit finite-difference scheme with eigenvalue perturbation. Geophysics **83 (6)**: A93–A98.

Geller RJ, and Takeuchi N (1998). Optimally accurate second-order time-domain finite difference scheme for the elastic equation of motion: one-dimensional cases. Geophys J Int **135**: 48–62.

Kelly K, Ward R, Treitel S, and Alford R (1976). Synthetic seismograms: A finite-difference approach. Geophysics **41**(1): 2–27.

Koene EF, Robertsson JO, Broggini F, and Andersson F (2017). Eliminating time dispersion from seismic wave modeling. Geophys J Int **213**: 169–180.

Lax P, and Wendroff B (1960). Systems of conservation laws. Communications on Pure and Applied Mathematics **13**: 217–237.

Lele SK (1992). Compact finite difference schemes with spectral-like resolution. Journal of Computational Physics **103 (1)**: 16–42.

Li X, Sarris CD, and Triverio P (2014) Overcoming the FDTD stability limit via model order reduction and eigenvalue perturbation. IEEE MTT-S International Microwave Symposium.: 1-3. 1-6 June 2014, Tampa, FL, USA. IEEE, USA.

Lines LR, Slawinski R and Bording R P (1999). A recipe for stability of finite-difference wave-equation computations. Geophysics **64**(3): 967–969.

Liu HF, Dai NX, Niu FL, and Wu W (2014). An explicit time evolution method for acoustic wave propagation. Geophysics **79**(3): T117–T124.

Liu Y (1998). Finite-difference numerical modeling of any even order accuracy. Oil Geophysical Prospecting **33**: 1–10 (in Chinese with English abstract).

Liu Y (2013). Globally optimal finite-difference schemes based on least squares. Geophysics **78**(4): T113–T132.

Liu Y, and Sen MK (2009a). An implicit staggered-grid finite-difference method for seismic modelling. Geophys J Int **179**:

459–474.

Liu Y, and Sen MK (2009b). A new time-space domain high-order finite-difference method for the acoustic wave equation. Journal of Computational Physics **228**(23): 8 779–8 806.

Liu Y, and Sen MK (2009c). A practical implicit finite-difference method: Examples from seismic modelling. J Geophys Eng **6**: 231–249.

Liu Y and Sen MK (2011). Finite-difference modeling with adaptive variable-length spatial operators. Geophysics **76**: T79–T89.

Liu Y and Sen MK (2013). Time-space domain dispersion-relation-based finite-difference method with arbitrary even-order accuracy for the 2D acoustic wave equation. Journal of Computational Physics **232**: 327–345.

Long GH, Zhao YB, and Zou J (2013). A temporal fourth-order scheme for the first-order acoustic wave equations. Geophys J Int **194**: 1 473–1 485.

McMechan GA (1983). Migration by extrapolation of time-dependent boundary values. Geophysical Prospecting **31**: 413–420.

Mitchell AR, and Griffiths DF (1980) The finite difference method in partial differential equations. John Wiley & Sons, New York, pp. 201.

Moczo P, Kristek J, Vavrycuk V, Archuleta R, and Halada L (2002). 3D heterogeneous staggered-grid finite-difference modeling of seismic motion with volume harmonic and arithmetic averaging of elastic moduli and densities. Bull Seismol Soc Amer **92**: 3 042–3 066.

Moczo P, Kristek J, and Gális M (2014) The finite-difference modelling of earthquake motions: Waves and ruptures. Cambridge University Press Cambridge University Press, United Kingdom, pp. 83.

Qu YM, Li ZC, Huang JP, Li JL, and Guan Z (2017). Elastic full-waveform inversion for surface topography. Geophysics **82**: R269–R285.

Ren ZM, and Li ZC (2017). Temporal high-order staggered-grid finite-difference schemes for elastic wave propagation. Geophysics **82**: T207–T224.

Ren ZM, Li ZC, Liu Y, and Sen MK (2017). Modeling of the acoustic wave equation by staggered-grid finite-difference schemes with high-order temporal and spatial accuracy. Bull Seismol Soc Amer **107**: 2 160–2 182.

Song XL, Fomel S, and Ying LX (2013). Lowrank finite-differences and lowrank Fourier finite-differences for seismic wave extrapolation in the acoustic approximation. Geophys J Int **193**: 960–969.

Tan SR, and Huang LJ (2014). An efficient finite-difference method with high-order accuracy in both time and space domains for modelling scalar-wave propagation. Geophys J Int **197**: 1 250–1 267.

Tarantola A (1984). Inversion of seismic reflection data in the acoustic approximation. Geophysics **49**: 1 259–1 266.

Virieux J (1984). SH-wave propagation in heterogeneous media: Velocity-stress finite-difference method. Geophysics **49**: 1 933–1 942.

Wang EJ, Ba J, and Liu Y (2018). Time-space-domain implicit finite-difference methods for modeling acoustic wave equations. Geophysics **83**: T175–T193.

Wang EJ, and Liu Y (2018). An implicit spatial and high-order temporal finite difference scheme for 2D acoustic modelling. Exploration Geophysics **49**: 187–201.

Wang EJ, Liu Y, and Sen MK (2016). Effective finite-difference modelling methods with 2-D acoustic wave equation using a combination of cross and rhombus stencils. Geophys J Int **206**: 1 933–1 958.

Xu SG, and Liu Y (2018). 3D acoustic wave modeling with a time-space-domain temporal high-order finite-difference scheme. J Geophys Eng **15**: 1 963–1 976.

Yang DH, He XJ, Ma X, Zhou YJ, and Li JS (2016). An optimal nearly analytic discrete-weighted Runge-Kutta discontinuous Galerkin hybrid method for acoustic wavefield modeling. Geophysics **81**: T251–T263.

Zhang JH, and Yao ZX (2012). Optimized finite-difference operator for broadband seismic wave modeling. Geophysics **78 (1)**: A13–A18.

Zhou HY, Liu Y, and Wang J (2018) Finite-difference modeling with adaptive variable-length temporal and spatial operators. 88th Annual International Meeting, SEG, Expanded Abstracts: 4015-4019.

Zhou HY, Liu Y, and Wang J (2021). Optimizing orthogonal-octahedron finite-difference scheme for 3D acoustic wave modeling by combination of Taylor-series expansion and Remez exchange method. Exploration Geophysics **52**(3): 335–355.

Zhou HB and Zhang G (2011). Prefactored optimized compact finite-difference schemes for second spatial derivatives. Geophysics **76**(5): WB87–WB95.